Pergamon

Bioorganic & Medicinal Chemistry, Vol. 5, No. 6, pp 1137–1147, 1997

PII: S0968-0896(97)00050-3
0968-0896/97 $17.00 + 0.00

Modulation of Nucleic Acid Structure by Ligand Binding: Induction of a DNA·RNA·DNA Hybrid Triplex by DAPI Intercalation

Zhitao Xu,[a] Daniel S. Pilch,[b,a,c] A. R. Srinivasan,[a] Wilma K. Olson,[a] Nicholas E. Geacintov[d] and Kenneth J. Breslauer[a,c,*]

[a]*Department of Chemistry, Rutgers—The State University of New Jersey, New Brunswick, NJ 08903, U.S.A.*
[b]*Department of Pharmacology, University of Medicine and Dentistry of New Jersey, Robert Wood Johnson Medical School, Piscataway, NJ 08854, U.S.A.*
[c]*The Cancer Institute of New Jersey, New Brunswick, NJ 08901, U.S.A.*
[d]*Department of Chemistry, New York University, New York, NY 10003, U.S.A.*

Abstract—The aromatic diamidine, DAPI (4′,6-diamidino-2-phenylindole), is used as an important biological and cytological tool since it forms highly fluorescent complexes with nucleic acid duplexes via minor groove-directed/intercalative modes of interaction. In this study, we find that DAPI binding can induce the formation of an RNA–DNA hybrid triplex that would not otherwise form. More specifically, through application of a broad range of spectroscopic, viscometric, and molecular modeling techniques, we demonstrate that DAPI intercalation induces the formation of the poly(dT)·poly(rA)·poly(dT) hybrid triple helix, a structure which does not form in the absence of the ligand. Using UV mixing studies, we demonstrate that, in the presence of DAPI, the poly(rA)·poly(dT) duplex and the poly(dT) single strand form a 1:1 complex (a triplex) that does not form in the absence of DAPI. Through temperature-dependent absorbance measurements, we show that the poly(dT)·poly(rA)·poly(dT) triplex melts via two distinct transitions: initial conversion of the triplex to the duplex state, with the DAPI remaining bound, followed by denaturation of the duplex–DAPI complex to its component single strands and free DAPI. Using optical melting profiles, we show that DAPI binding enhances the thermal stability of the poly(dT)·poly(rA)·poly(dT) triplex, an observation consistent with the preferential binding of the ligand to the triplex versus the duplex and single-stranded states. Our differential scanning calorimetric measurements reveal melting of the DAPI-saturated poly(dT)·poly(rA)·poly(dT) triplex to be associated with a lower enthalpy but greater cooperativity than melting of the corresponding DAPI-saturated poly(rA)·poly(dT) duplex. Our flow linear dichroism and viscometric data are consistent with an intercalative mode of binding when DAPI interacts with both the poly(dT)·poly(rA)·poly(dT) triplex and the poly(rA)·poly(dT) duplex. Finally, computer modeling studies suggest that a combination of both stacking and electrostatic interactions between the intercalated ligand and the host nucleic acid play important roles in the DAPI-induced stabilization of the poly(dT)·poly(rA)·poly(dT) triplex. In the aggregate, our results demonstrate that ligand binding can be used to induce the formation of triplex structures that do not form in the absence of the ligand. This triplex-inducing capacity has potentially important implications in the design of novel antisense, antigene, antiviral, and diagnostic strategies. © 1997 Elsevier Science Ltd.

Introduction

The recognition of the potential biological roles and biomedical applications of triplex structures has focused considerable attention on the triple-helical forms of nucleic acids, as well as on their interactions with nucleic acid-binding ligands.[1–7] Recent biomedical applications of triplex structures include the specific control of cellular processes, such as transcription and replication,[2,5,8–17] as well as the mapping of megabase DNA through the selective cleavage of specific DNA duplex domains.[18–26] The effective development of such applications requires a database that allows one to predict/control the affinities and specificities of third-strand probes for target DNA·DNA, RNA·RNA and RNA·DNA duplex domains. In recognition of this need, several studies have focused on elucidating the influence of 'strand composition' (RNA versus DNA) on the stabilities and energetics of triplex structures.[27–29] Significantly, these studies revealed that triplex formation favors RNA in both pyrimidine strands and DNA in the purine strand, with no observation of a DNA(pyrimidine)·RNA(purine)·DNA(pyrimidine) triplex. Recently, we reported that this RNA–DNA, hybrid type of triplex could, in fact, be *induced* by a range of nucleic acid-binding ligands.[30] Specifically, we showed that binding by the ligands, DAPI, berenil, ethidium, and netropsin, could induce formation of the poly(dT)·poly(rA)·poly(dT) triplex (hereafter abbreviated to poly(rA)·2poly(dT)). However, comparatively little is known about the physiochemical properties that govern these triplex-stabilizing binding events. This deficiency limits our understanding of the molecular forces that control the relative triplex-inducing efficiency of a ligand, which, in turn, constrains our ability to define solution conditions and structural modifications which could predictably alter triplex-stabilizing/inducing properties. To alleviate this situation, we have begun a program in which we are characterizing the

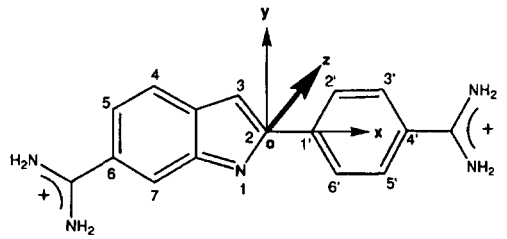

Figure 1. Chemical structure of DAPI (4′,6-diamidino-2-phenylindole) indicating the atomic numbering as well as the *x*, *y*, *z* coordinate reference frame used in model building.

influences of various nucleic acid-binding ligands on the formation and properties of DNA, RNA, and RNA–DNA hybrid triplexes.

In this article, we describe how one can use a broad range of spectroscopic, calorimetric, and computer modeling techniques to study the impact of DAPI (Fig. 1) binding on the formation of the poly(rA)·2poly(dT) triplex, while characterizing both the mode of DAPI complexation with this nucleic acid structure and the melting energetics of the resulting DAPI-poly- (rA)·2poly(dT) complex. Our results reveal that DAPI exhibits properties characteristic of intercalation when complexed with the poly(rA)·2poly(dT) triplex, while providing evidence for the ability of such a ligand to alter dramatically the affinity and specificity of a third strand for its host duplex. This capacity of a ligand to modulate triplex formation provides a new strategy for the rational design of novel antisense, antigene, antiviral, and diagnostic agents.

Results and Discussion

Stoichiometry of the complex formed by poly(rA)·poly(dT) and poly(dT)

To establish the stoichiometry of the complex, if any, formed by mixing solutions of the poly(rA)·poly(dT) duplex and the poly(dT) single strand in the absence and presence of ligand, we used the method of continuous fractions.[31] The resulting mixing curves determined at 260 nm for poly(rA)·poly(dT) and poly(dT) in the absence and presence of DAPI are shown in Figure 2 and discussed below.

DAPI binding induces formation of the poly(rA)·2poly(dT) triplex, a complex which does not form in the absence of the ligand. Inspection of the mixing curves in Figure 2 reveals that, in the absence of ligand, no inflection point is observed. This observation suggests that single-stranded poly(dT) does not hybridize with the poly(rA)·poly(dT) duplex. Thus, in the absence of ligand, the poly(rA)·2poly(dT) triplex is not formed under the solution conditions employed here (110 mM Na^+, pH 6.8). Further inspection of Figure 2, however, reveals that in the presence of DAPI, a single inflection point is observed at 46.9% poly(dT), consistent with formation of a 1:1 complex between poly(dT) and poly(rA)·poly(dT), which we propose

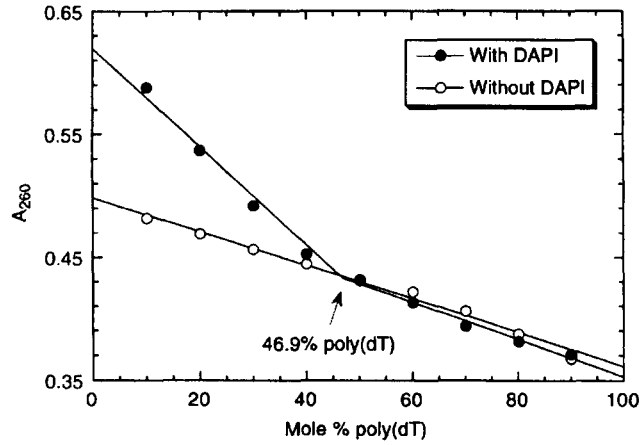

Figure 2. Absorbance mixing curves at 260 nm showing the stoichiometry of complexes formed by poly(rA)·poly(dT) and poly(dT) in the absence (○) and presence (●) of DAPI (at a [total DAPI] to [nucleotide] ratio of 0.17). Solution conditions are 10 mM sodium cacodylate (pH 6.8), 100 mM NaCl, and 0.1 mM EDTA.

corresponds to the poly(rA)·2poly(dT) triplex. In short, the two mixing curves are consistent with DAPI binding inducing the formation of the poly(rA)·2poly(dT) triplex.

Thermally induced denaturation of the complex as measured by UV absorbance

We used temperature-dependent UV absorbance measurements at 260 nm to monitor the thermally induced denaturation of the complex formed by poly(rA)·poly(dT) and poly(dT) in the absence and presence of differing concentrations of DAPI. The resulting melting curves are shown in panel A of Figure 3 and discussed below.

In the absence of DAPI, only the poly(rA)·poly(dT) duplex to single strand transition is observed. Inspection of the solid line melting profile (corresponding to a [total DAPI]/[base triplet] ratio (r_{bt}) of 0) in panel A of Figure 3 reveals that, in the absence of ligand, a solution containing a 1:1 stoichiometry of poly(rA)·poly(dT) and poly(dT) exhibits a single Watson–Crick (WC) transition (T_{max} = 64.6 °C). This transition corresponds to the well-known denaturation of the poly(rA)·poly(dT) duplex.[32,33] This assignment is consistent with the corresponding mixing curve (Fig. 2), which also reveals that, in the absence of ligand, the poly(rA)·2poly(dT) triplex is not formed under the solution conditions employed here (110 mM Na^+, pH 6.8). In other words, poly(dT) remains as an unhybridized single strand, an observation that agrees with the independent findings of the Crothers, Dervan, and Hélène groups,[27–29] who have shown that a pyrimidine DNA third strand will not bind to a hybrid duplex containing a purine RNA strand.

In the presence of DAPI, two melting transitions are observed: the poly(rA)·2poly(dT) triplex to poly(rA)·poly(dT) duplex transition followed by the poly(rA)·poly(dT) duplex to single strand transition. In contrast to the single transition in the melting profile of

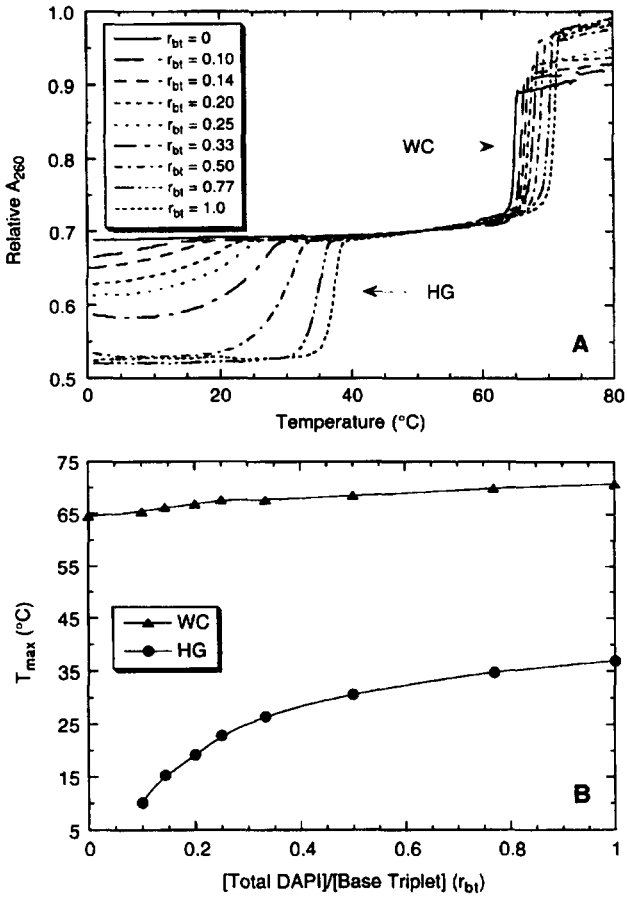

Figure 3. (A) UV melting profiles at 260 nm of solutions containing a 1:1 stoichiometric mixture of poly(dT) and poly(rA)·poly(dT) in the absence and presence of DAPI at the indicated values of r_{bt} (defined as the [total DAPI] to [base triplet] ratio). (B) T_{max} versus r_{bt} profiles for the thermal transitions of the melting profiles in panel A. Solution conditions are as described in the legend to Figure 2.

the solution containing a 1:1 stoichiometry of poly(rA)·poly(dT) and poly(dT), we observe two transitions in each of the melting profiles in the presence of DAPI (Fig. 3A). One of these transitions (T_{max} ranging from 65.4 to 70.8 °C) corresponds to the expected WC transition, which reflects denaturation of the poly(rA)·poly(dT) duplex into its component single strands. We assign the second DAPI-induced transition (T_{max} ranging from 10.1 to 37.0 °C) to the dissociation of poly(dT) from the poly(rA)·poly(dT) duplex (the Hoogsteen (HG) transition). This assignment is consistent with the mixing curve results shown in Figure 2, which reveal that DAPI binding induces formation of the poly(rA)·2poly(dT) triplex. In short, for the solution containing a 1:1 stoichiometry of poly(rA)·poly(dT) and poly(dT), both the mixing curves and the melting profiles are consistent with formation of the poly(rA)·2poly(dT) triple-helical complex in the presence of DAPI.

Further inspection of the melting curves in panel A of Figure 3 reveals that both the sharpness and hyperchromicity of the HG transition increase as r_{bt} increases from 0.1 to 0.50. We find that r_{bt} ratios above 0.5 do not result in further increases in transition hyperchromicity, while inducing only marginal increases in transition sharpness. These observations may reflect partial formation of the poly(rA)·2poly(dT) triplex at r_{bt} ratios below 0.50, with complete triplex formation occurring only at r_{bt} ratios $\geq$0.50. In this interpretation, the partially formed triplex would exhibit a lower apparent melting cooperativity compared with the fully formed triplex. An alternative explanation invokes a fully formed poly(rA)·2poly(dT) triplex whose melting cooperativity increases with increasing DAPI binding density. Both of these possibilities could, in principle, give rise to the observed dependence on r_{bt} of the sharpness and hyperchromicity of the HG transition.

DAPI binding enhances the thermal stability of the poly(rA)·2poly(dT) triplex. Panel B of Figure 3 shows the correlation between r_{bt} and the T_{max} values of the melting profiles presented in panel A of Figure 3. Note that DAPI binding thermally stabilizes both the triplex to duplex and the duplex to single strand equilibria, with the extent of these thermal enhancements being greater for the triplex to duplex transition (ΔT_{max} > 34.8 °C at a r_{bt} ratio of 0.77) than for the duplex to single strand transition (ΔT_{max} = 5.3 °C at a r_{bt} ratio of 0.77). These observations are consistent with a model in which the DAPI binding affinity follows the hierarchy: poly(rA)·2poly(dT) triplex > poly(rA)·poly(dT) duplex > poly(dT) and poly(rA) single strands. Thus, for the RNA–DNA hybrid system studied here, DAPI preferentially complexes with the triplex relative to the duplex or single-stranded states. To the best of our knowledge, our observation of ligand-induced changes in the thermal stabilities of the poly(rA)·2poly(dT) triplex and the poly(rA)·poly(dT) duplex provides the first demonstrations of DAPI binding to RNA–DNA hybrid duplex and triplex structures.

The results presented and discussed above describe our use of UV absorbance measurements to define the nature and thermal stability of the complex formed by poly(rA)·poly(dT) and poly(dT) in the presence of DAPI. In the section that follows, we describe our use of calorimetric techniques to characterize the melting energetics of that complex.

Thermally induced denaturation of an RNA·DNA duplex in the absence of DAPI and a DNA·RNA·DNA triplex in the presence of DAPI as measured by DSC

We have used DSC to measure the enthalpy change associated with the thermally induced transitions of a solution containing a 1:1 stoichiometry of poly(rA)·poly(dT) and poly(dT) in the absence and presence of bound DAPI (at r_{bt} = 1.0). The resulting thermograms are shown in panels A and B of Figure 4 and discussed below.

Calorimetric detection of the Hoogsteen triplex transition in addition to the Watson–Crick duplex transition requires the presence of DAPI. In the absence of ligand, a solution containing a 1:1 stoichiometry of

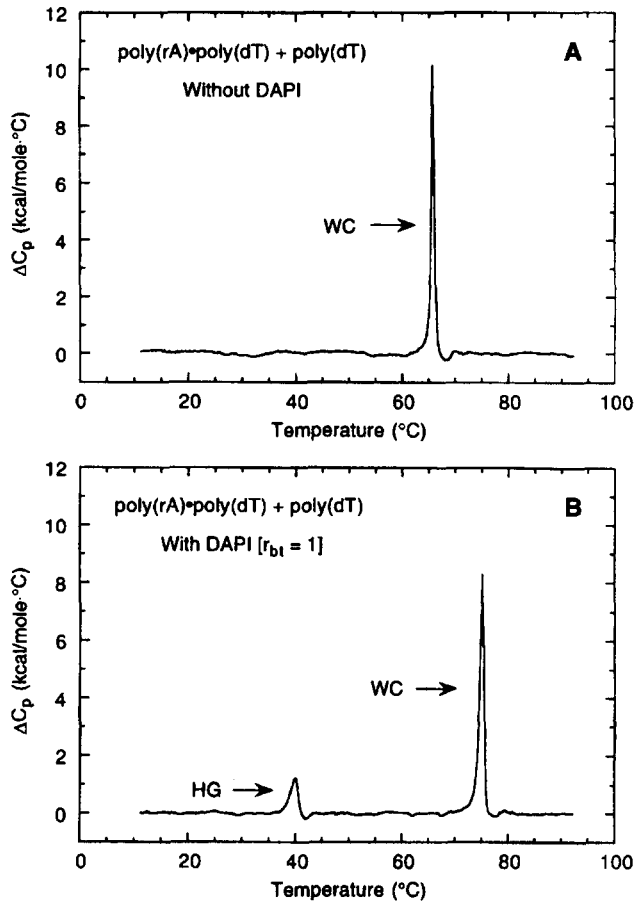

Figure 4. Excess heat capacity (ΔC_p) versus temperature profiles of solutions containing a 1:1 stoichiometric mixture of poly(rA)·poly(dT) and poly(dT) in the absence (A) and presence (B) of DAPI at an r_{bt} ratio of 1.0. Nucleic acid concentrations are 0.3 mM in nucleotide. Solution conditions are as described in the legend to Figure 2; r_{bt} is as defined in the legend to Figure 3.

poly(rA)·poly(dT) and poly(dT) exhibits a single peak corresponding to the WC transition (Fig. 4A). This DSC result in the absence of ligand is consistent with the corresponding mixing curve (Fig. 2) and UV melting profile (Fig. 3A), which also reveal that, in the absence of ligand, the poly(rA)·2poly(dT) triplex is not formed under the solution conditions employed here (110 mM Na^+, pH 6.8). By contrast, in the presence of DAPI (Fig. 4B), we observe two DSC peaks corresponding to both the HG and WC transitions. Thus, for the solution containing a 1:1 stoichiometry of poly(rA)·poly(dT) and poly(dT) in the presence of DAPI, the UV mixing curves, the UV melting profiles, and the DSC thermograms all reveal formation of the poly(rA)·2poly(dT) triple-helical complex.

The enthalpy of triplex melting in the presence of DAPI. The enthalpy data derived from integration of the DSC peaks shown in Figure 4 are listed in Table 1. Inspection of these data reveals that, when DAPI is bound, the poly(rA)·2poly(dT) triplex to poly(rA)·poly(dT) duplex (HG) transition is associated with an endothermic enthalpy change (ΔH_{cal}) of 3.0 kcal per mol base triplet (bt). This heat of triplex melting should not be regarded as representing the HG transition enthalpy of the DAPI-free triplex, since it potentially includes any differential enthalpic contributions ($\Delta\Delta H$) from DAPI binding to the triplex versus the duplex states. Knowledge of the nature of this differential enthalpic contribution would enable us to assess whether our measured enthalpy change for the melting of the DAPI-bound triplex can be considered as an upper or lower limit to the HG transition enthalpy of the DAPI-free triplex. Unfortunately, the inability of poly(dT) to hybridize with the poly(rA)·poly(dT) duplex in the absence of DAPI precludes us from defining the nature of the differential enthalpic contribution from DAPI binding to the poly(rA)·2poly(dT) triplex versus the poly(rA)·poly(dT) duplex.

The DAPI-bound triplex melts more cooperatively than the DAPI-bound duplex. As noted above, we have used DSC to measure the enthalpy change (ΔH_{cal}) associated with the thermally induced transitions (HG/WC) of a solution containing a 1:1 stoichiometry of poly(rA)·poly(dT) and poly(dT) in both the absence and presence of bound DAPI. We also have derived the corresponding van't Hoff transition enthalpies (ΔH_{vH}) by analyzing the shapes of the first derivatives of the UV melting profiles. Due to the pseudomonomolecular nature of the transitions, which exhibit no concentration dependence, we assumed a molecularity of one for this analysis. For each transition, the ratio of ΔH_{vH} to ΔH_{cal} provides a measure of the cooperativity of the melting event.[34] These data are summarized in Table 1. Inspection of these data reveals that, in the presence of bound DAPI, the HG transition of the poly(rA)·2poly(dT) triplex exhibits a cooperative unit of 95 bt, while the WC transition exhibits a cooperative unit of only 76 base pairs (bp). Although these

Table 1. Calorimetric and van't Hoff transition enthalpies for the DAPI-saturated poly(rA)·2poly(dT) triplex and for the corresponding DAPI-free and DAPI-saturated poly(rA)·poly(dT) duplexes[a]

Transition	r_{bt} or r_{bp}	ΔH_{cal}[b] (kcal/mol bt or bp)	ΔH_{vH}[c] (kcal/mol bt or bp)	$\Delta H_{vH}/\Delta H_{cal}$ (cooperative unit)
(rA)·2(dT) → (rA)·(dT) + (dT)	1.0	3.0	284	95
(rA)·(dT) + (dT) → (rA) + 2(dT)	0	8.3	1017	123
(rA)·(dT) + (dT) → (rA) + 2(dT)	1.0	10.2	778	76

[a]Solution conditions were 10 mM sodium cacodylate (pH 6.8), 100 mM NaCl, and 0.1 mM EDTA.
[b]Calorimetric transition enthalpies (ΔH_{cal}) were calculated from the areas under ΔC_p vs temperature curves, with an uncertainty in the data of <5%.
[c]The van't Hoff transition enthalpies (ΔH_{vH}) were calculated from the shapes of the first derivatives of UV melting curves, with an assumed molecularity of one[54] and an uncertainty in the data of <10%.

differences are close to the experimental uncertainty due to the error inherent in the van't Hoff analysis, it appears that the DAPI-bound poly(rA)·2poly(dT) triplex melts more cooperatively than the corresponding DAPI-bound poly(rA)·poly(dT) duplex. We previously have observed similar ligand-induced changes in melting cooperativities for both the poly(dA)·2poly(dT) DNA triplex and the poly(rA)·2poly(rU) RNA triplex in the absence and presence of bound berenil, a chemically similar drug to DAPI.[35] This study extends these observations to RNA–DNA hybrid duplexes and triplexes.

Further inspection of the data in Table 1 reveals that, in the presence of bound DAPI, the WC transition exhibits a cooperative unit of 76 bp, in contrast to a cooperative unit of 123 bp in the absence of bound DAPI. Thus, DAPI binding decreases the melting cooperativity of the poly(rA)·poly(dT) duplex, an observation previously noted in this laboratory in studies probing the interactions of both intercalating and minor groove-directed ligands with various DNA and RNA host duplexes.[33,36–41] Unfortunately, we are unable to determine the effect of DAPI binding on the melting cooperativity of the poly(rA)·2poly(dT) triplex, due to the inability of poly(dT) and poly(rA)·poly(dT) to form the poly(rA)·2poly(dT) triple-helical complex in the absence of bound DAPI.

In the next section, we characterize further the physiochemical properties of the DAPI-induced poly(rA)·2poly(dT) triplex by mapping the salt dependence of its thermal stability (T_m).

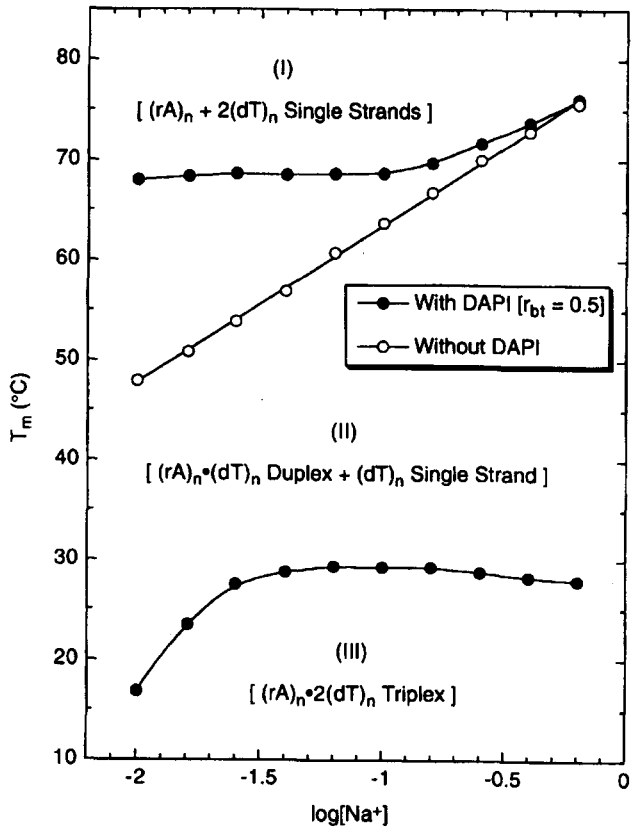

Figure 5. Phase diagram which maps T_m versus log[Na^+] for a 1:1 stoichiometric mixture of poly(rA)·poly(dT) and poly(dT) in the absence (○) and presence (●) of DAPI at an r_{bt} ratio of 0.5. The structural states which correspond to each phase (I, II, or III) are indicated. Buffer conditions are 10 mM sodium cacodylate (pH 6.8–6.9) and 0.1 mM EDTA; r_{bt} is as defined in the legend to Figure 3.

Phase diagram of the DAPI-induced poly(rA)·2poly(dT) triplex

We have used temperature-dependent UV absorbance measurements to determine a phase diagram for a 1:1 stoichiometric mixture of poly(rA)·poly(dT) and poly(dT) in the absence and presence of bound DAPI (at a r_{bt} ratio of 0.50). Specifically, we mapped the dependence on Na^+ concentration of the thermal stabilities (T_m) of the following two transitions:

$$\text{poly(rA)} \cdot 2\text{poly(dT)} \rightarrow \text{poly(dT)} + \text{poly(rA)} \cdot \text{poly(dT)} \quad [HG]$$

$$\text{poly(rA)} \cdot \text{poly(dT)} + \text{poly(dT)} \rightarrow \text{poly(rA)} + 2\text{poly(dT)} \quad [WC]$$

The resulting phase diagrams are shown in Figure 5. Such phase diagrams are important for defining and comparing the nucleic acid-binding properties of DAPI over a range of solution conditions.

Inspection of Figure 5 reveals that, in the absence of DAPI, only a WC transition is observed over the range of Na^+ concentrations studied (10–631 mM). This observation is consistent with a previous study,[32] in which formation of the poly(rA)·2poly(dT) triplex was shown to require Na^+ concentrations in excess of 2.5 M. In contrast to the phase diagram in the absence of DAPI, the phase diagram in the presence of DAPI includes both HG and WC transitions, consistent with the UV mixing curves (Fig. 2) and calorimetric (Fig. 4) melting profiles described above.

Inspection of this phase diagram reveals that increasing the Na^+ concentration from 10 mM (log[Na^+] = −2.0) to 63 mM (log[Na^+] = −1.2) causes the T_m value of the HG transition (phase III to phase II) to increase by 12.5 °C. Thus, at Na^+ concentrations below 63 mM, addition of Na^+ ions thermally stabilizes the poly(rA)·2poly(dT) triplex in a manner that is both additive and synergistic with the thermally stabilizing effects of the bound ligand. By contrast to the effects of Na^+ ions at concentrations below 63 mM (log[Na^+] < −1.2), increasing the Na^+ concentration from 158 mM (log[Na^+] = −0.80) to 631 mM (log[Na^+] = −0.20) causes the T_m value of the HG transition to decrease by 1.4 °C. This decrease in thermal stability may reflect a Na^+-induced reduction in the extent of DAPI binding to the poly(rA)·2poly(dT) triplex (see Fig. 3), with the higher Na^+ concentration being unable to compensate fully the loss in triplex thermal stability resulting from ligand expulsion. Between the Na^+ concentrations of 63 mM (log[Na^+] = −1.2) and 158 mM (log[Na^+] =

−0.80), the T_m value of the HG transition remains essentially unchanged. Thus, over this narrow range of Na^+ concentrations, the loss in triplex thermal stability that accompanies any Na^+-induced ligand expulsion is compensated by the salt-induced enhancement of thermal stability.

Further inspection of Figure 5 reveals that, at Na^+ concentrations below 631 mM ($\log[Na^+] = -0.20$), addition of DAPI causes the T_m values of WC transitions (phase II to phase I) to increase. Furthermore, at Na^+ concentrations <100 mM ($\log[Na^+] < -1.0$), the slopes of the lines, $\delta T_m/\delta\log[Na^+]$, that separate phases I and II (which correspond to the WC transitions) are quite different for the ligand-free and ligand-bound poly(rA)·poly(dT) duplexes, (15.0 °C for the ligand-free duplex and 0.7 °C for the ligand-bound duplex). By contrast, at Na^+ concentrations between 100 mM ($\log[Na^+] = -1.0$) and 631 mM ($\log[Na^+] = -0.20$), the $\delta T_m/\delta\log[Na^+]$ value for the WC transition line of the ligand-bound duplex (10.7 °C) approaches that of the ligand-free duplex (15.0 °C). This observation may reflect a salt-induced reduction in the extent of DAPI binding to the poly(rA)·poly(dT) duplex at Na^+ concentrations above 100 mM, with control of duplex thermal stability being governed by the Na^+ concentration rather than the bound ligand. Thus, the differential $\delta T_m/\delta\log[Na^+]$ values at Na^+ concentrations below and above 100 mM may well reflect the differential salt dependencies of the thermal stabilities of the DAPI-bound and the DAPI-free poly(rA)·poly(dT) duplexes.

In the preceding sections we described our use of UV absorbance and calorimetric measurements to define the thermal stability, phase diagram, and melting energetics of the DAPI-bound poly(rA)·2poly(dT) triplex. In the sections that follow, we describe our use of flow linear dichroism and viscometric techniques to characterize the mode by which DAPI complexes with the poly(rA)·2poly(dT) triplex.

Flow linear dichroism measurements are consistent with DAPI intercalation into the poly(rA)·2poly(dT) triplex

Flow linear dichroism is a useful technique for defining the mode by which a ligand is complexed with a host nucleic acid structure.[42] Linear dichroism (LD) is defined by the relationship

$$LD = A_{\parallel} - A_{\perp} \qquad (1)$$

where $A_{\parallel}$ and $A_{\perp}$ denote, respectively, the sample absorbances with the polarization vectors of the light oriented either in a parallel or a perpendicular orientation with respect to the flow lines. When the transition dipole moment of a singly oriented chromophore (e.g., a DNA base and/or a bound aromatic ligand) lies within the plane of the molecule and makes an angle, θ, with the orientation axis, this angle can be related to the reduced linear dichroism, LD^r, by the equation[42–44]

$$LD^r = \frac{LD}{A} = \frac{3}{2}(3\cos^2\theta - 1)F(G) \qquad (2)$$

where A is the isotropic absorbance of the sample and $F(G)$ is an orientation factor, which has values in the range of $0 < F(G) < 1$. Equation (2) implies that a positive LD^r signal is associated with an angle θ of <55°, while a negative LD^r signal is associated with an angle θ of >55°. In a typical flow LD experiment, the long axis of the nucleic acid helix is aligned along the flow lines.[42–44] Thus, the nucleic acid bases, which are oriented roughly perpendicular to the helix axis (i.e., $\theta_{bases} \approx 90$ °C), give rise to a negative LD^r signal. A drug molecule that is bound to the minor groove of a nucleic acid structure typically exhibits an angle θ_{drug} of approximately 40–50° relative to the helix axis, and therefore gives rise to a positive LD^r signal. In contrast to a minor groove-bound drug molecule, an intercalated drug molecule, like the nucleic acid bases, is oriented roughly perpendicular to the helix axis ($\theta_{drug} \approx 90$ °C), and therefore give rise to a negative LD^r signal.

Figure 6 shows the absorbance (panel A) and LD^r (panel B) spectra of a DAPI–poly(rA)·2poly(dT) complex at a r_{bt} ratio of 0.5. For comparative purposes, the absorbance (panel A) and LD^r (panel B) spectra of a DAPI–poly(rA)·poly(dT) complex at a [total DAPI] to [base pair] ratio (r_{bp}) of 0.2 are also shown. Inspection of Figure 6 reveals that, as expected, the LD^r spectra of both the DAPI–poly(rA)·2poly(dT) and the DAPI–poly(rA)·poly(dT) complex are negative in the 240–300 nm wavelength region where the nucleic acid absorbs. As observed for the LD^r spectra in this DNA-absorbing region, the LD^r spectra of both the DAPI–poly(rA)·2poly(dT) and DAPI–poly(rA)·poly(dT) complexes are also negative in the 300–380 nm drug-absorbing wavelength region. These negative LD^r signals are consistent with DAPI intercalation into both the poly(rA)·2poly(dT) triplex and the poly(rA)·poly(dT) duplex. We recognize that such negative LD^r signals also might arise from a non-specific, electrostatically driven mode of binding in which the DAPI molecules are stacked along the helix exterior, with their long axes (denoted by the X-axis in Fig. 1) oriented roughly perpendicular to the helix axis. However, the persistence of the HG melting transition of the DAPI–poly(rA)·2poly(dT) complex at Na^+ concentrations as high as 631 mM (see Fig. 5) suggests a mode of ligand binding that is not driven by simple electrostatic interactions. In this connection, the Wilson and Nordén groups previously have shown that DAPI intercalates at $(dG\text{-}dC)_n\cdot(dG\text{-}dC)_n$ and $(rA)_n\cdot(rU)_n$ sites, while binding to the minor groove of $(dA)_n\cdot(dT)_n$, $(dI\text{-}dC)_n\cdot(dI\text{-}dC)_n$, and $(dA\text{-}dT)_n\cdot(dA\text{-}dT)_n$ sites.[45–49] Our observations suggest that potential sites for DAPI intercalation also should include the $(rA)_n\cdot(dT)_n$ and $(rA)_n\cdot 2(dT)_n$ hybrid sequences.

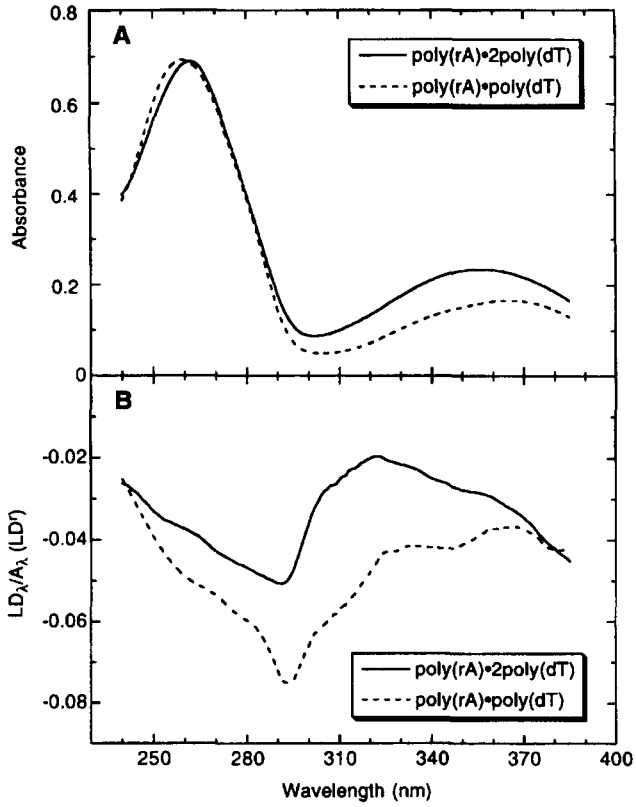

Figure 6. Isothermal absorption spectra (A) and reduced linear dichroism spectra (B) at 25 °C for the DAPI–poly(rA)·2poly(dT) complex at an r_{bt} ratio of 0.5 (—) and for the DAPI–poly(rA)·poly(dT) complex (- - -) at a r_{bp} ratio of 0.2. Solution conditions for the DAPI–poly(rA)·2poly(dT) complex are as described in the legend to Figure 2, while those for the DAPI–poly(rA)·poly(dT) complex are 10 mM sodium cacodylate (pH 6.8), 25 mM NaCl, and 0.1 mM EDTA. r_{bp} is the [total DAPI] to [base pair] ratio, while r_{bt} is as defined in the legend to Figure 3.

A recent LD study by Nordén and coworkers has indicated that DAPI binds to the minor groove of the all-DNA poly(dA)·2poly(dT) triplex.[48] This observation contrasts with the intercalative binding mode we observe here for DAPI complexation with the poly(rA)·2poly(dT) RNA–DNA hybrid triplex. Thus, DAPI is able to discriminate between the poly(dA)·2poly(dT) and poly(rA)·2poly(dT) triple-helical structures. The structural/energetic basis for this discrimination is difficult to discern since the poly(rA)·2poly(dT) triplex does not form in the absence of the ligand.

Viscometric measurements also are consistent with DAPI intercalation into the poly(rA)·2poly(dT) triplex

Viscometric measurements provide a second method for characterizing the mode of ligand binding that is independent of the optical properties of the ligand.[50] Ligand insertion between stacked bases within a linear host helix (intercalation) is associated with a lengthening of the nucleic acid. Thus, a ligand-induced increase in the viscosity of a nucleic acid solution is consistent with (but does not prove) an intercalative mode of binding. Conversely, the lack of a ligand-induced increase in the viscosity of a nucleic acid solution is consistent with (but does not prove) a non-intercalative binding mode, such as minor groove association.

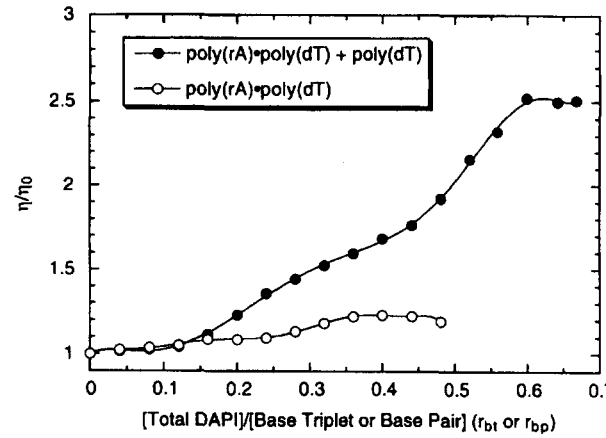

Figure 7. Viscometric titrations at 3.5 °C of either poly(rA)·poly(dT) (○) or a 1:1 stoichiometric mixture of poly(rA)·poly(dT) and poly(dT) (●) with DAPI. Solution conditions are as described in the legend to Figure 2.

Figure 7 shows the effect of DAPI binding on the relative solution viscosity (η/η_0) of the poly(rA)·poly(dT) duplex or of a 1:1 stoichiometric mixture of poly(rA)·poly(dT) and poly(dT). Note that on addition of DAPI, the solution viscosity of the poly(rA)·poly(dT) duplex increases to an extent which is $\approx$1.2-fold that of the ligand-free duplex. This increase in solution viscosity is consistent with some degree of DAPI intercalation into the poly(rA)·poly(dT) duplex. Further inspection of Figure 7 reveals that on addition of DAPI the solution containing the 1:1 stoichiometric mixture of poly(rA)·poly(dT) and poly(dT) undergoes a biphasic increase in viscosity to a final extent which is $\approx$2.5-fold that in the absence of ligand. The first phase of this viscosity increase occurs between r_{bt} ratios of 0 and 0.45, while the second phase occurs between r_{bt} ratios of 0.45 and 0.67. Recall that the r_{bt} dependence of the per cent hyperchromicity associated with the HG transition of the DAPI–poly(rA)·2poly(dT) complex is consistent with complete triplex formation occurring only at r_{bt} ratios $\gtrapprox$0.5 (see panel A of Fig. 3). Thus, the first phase of the observed increase in the viscosity of the solution containing the 1:1 stoichiometric mixture of poly(rA)·poly(dT) and poly(dT) probably correlates with DAPI-induced hybridization of the poly(dT) single strand with the poly(rA)·poly(dT) duplex to form the poly(rA)·2poly(dT) triplex. By contrast, the second phase of this viscosity increase is consistent with DAPI intercalation into the poly(rA)·2poly(dT) triplex. Thus, both the linear dichroism and viscometric data are consistent with intercalative properties for DAPI when complexed with either the poly(rA)·poly(dT) duplex or the poly(rA)·2poly(dT) triplex.

A potential structure for the DAPI–poly(rA)·2poly(dT) intercalated complex

The linear dichroism and viscometric results described in the preceding sections suggest that DAPI intercala-

tion induces the formation of the poly(rA)·2poly(dT) triplex. We have also studied the effect of a classic intercalating ligand, ethidium bromide, on formation of the poly(rA)·2poly(dT) triplex and found the resulting ethidium–poly(rA)·2poly(dT) complex to be ≈ 16 °C less thermally stable than the corresponding DAPI–poly(rA)·2poly(dT) complex.[30] Thus, based on the enhanced thermal stabilities of the drug-bound poly(rA)·2poly(dT) complexes, DAPI is a more efficient triplex inducer than ethidium. This observation suggests that the capacity of a ligand to induce the formation of triplex structures depends not only on the mode by which it binds, but also on the structural/conformational nature of the ligand–nucleic acid complex.

To gain insight into the potential structural nature of the DAPI–poly(rA)·2poly(dT) intercalated complex, we have used the computer modeling methods described in the Experimental section to explore the energetically feasible structures this complex might adopt. The lowest-energy structure to emerge from these studies is presented in Figure 8. Inspection of Figure 8 reveals a structure in which the indole ring of DAPI is stacked between adjacent, rA·dT WC base pairs, with the cationic 6-amidino group protruding into the major groove and the 2-(4′-amidino)phenyl moiety protruding into the minor groove. This structural model suggests that DAPI-induced stabilization of the poly(rA)·2poly(dT) triplex may be linked to the synergistic actions of two types of molecular interactions; namely, stacking interactions within the WC portion of the helix and attractive electrostatic interactions in the electronegative major and minor grooves. Thus, intercalation of the DAPI molecule between rA·dT WC base pairs may poise the rA bases for HG hydrogen bonding interactions with third-strand dT bases. In this model, electrostatic repulsion between the phosphates of the incoming third strand and those lining the major groove of the duplex would be minimized by the presence in the major groove of the cationic 6-amidino group of the bound DAPI.

Concluding remarks

In the study reported here, we have demonstrated that ligand binding can induce the formation of nucleic acid triplexes that otherwise would not form. Specifically, we have shown that DAPI intercalation can induce formation of the poly(rA)·2poly(dT) hybrid triplex. Thus, ligand binding can be used to overcome energetic barriers to the formation of specific triplex structures. Ligand-induced formation of new classes of hybrid triplexes may have implications in the recognition of RNA·DNA duplexes by cellular and viral proteins, such as ribonuclease H and reverse transcriptase.[51–53] Triplex formation at protein recognition sites may provide a means for specific control of protein function. The results presented here highlight the potential use of nucleic acid-binding ligands to modulate the affinities and specificities of third strands for their duplex targets. In this way, novel antisense, antigene, antiviral, and diagnostic strategies may be designed with greater degrees of specificity and perhaps even enhanced clinical efficacies.

Experimental

Nucleic acid and ligand molecules

Synthetic poly(rA) and poly(dT) were purchased from Pharmacia Biotech (Piscataway, NJ) and were used without further purification. DAPI was purchased from Sigma Chemical (St Louis, MO) and was also used without further purification. Concentrations of DAPI

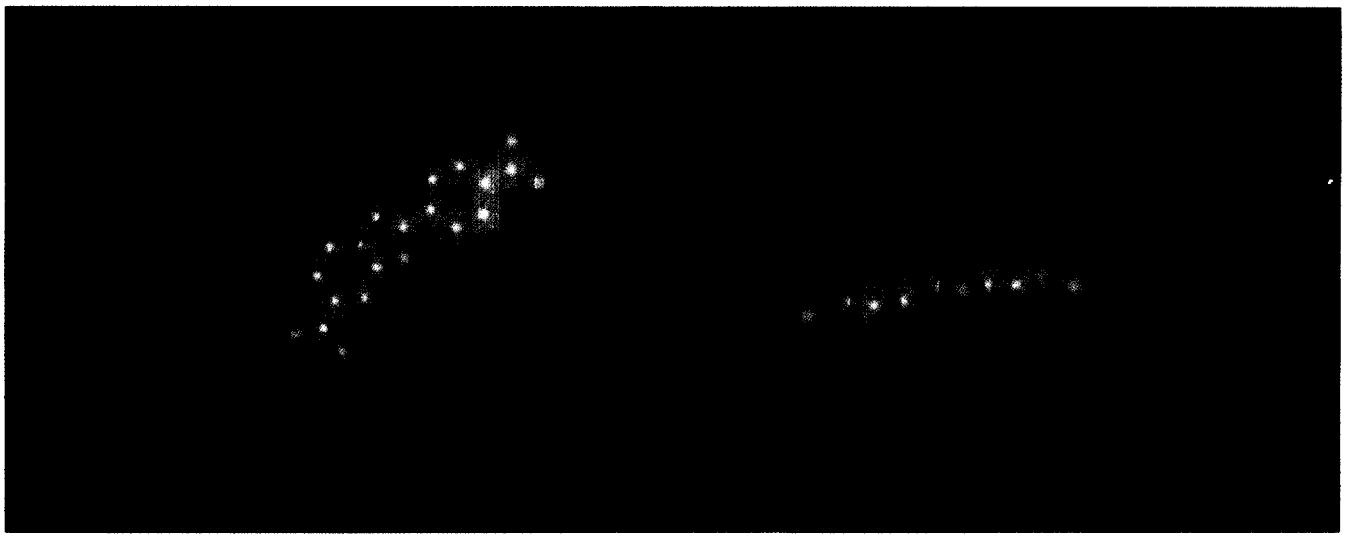

Figure 8. Lowest-energy model for the DAPI-poly(rA)·2poly(dT) intercalated complex. The WC-paired poly(rA) and poly(dT) strands are shown in purple and green, respectively, while the HG-paired poly(dT) third strand is shown in red. The van der Waals' radii of the carbon (chrome) and nitrogen (blue) atoms of DAPI are depicted by CPK surfaces. Left: Top view looking down the helix axis. Right: Side view looking into the minor groove.

and polymer stock solutions were determined spectrophotometrically.

UV spectrophotometry

All UV absorbance measurements were conducted on a computer-interfaced, dual-beam, Perkin–Elmer model Lambda 4C spectrophotometer, equipped with a thermoelectrically controlled cell holder. A quartz cell with a 1 cm pathlength was used for all the UV studies.

UV mixing curves. Isothermal (5 °C) UV mixing experiments were conducted in a pH 6.8, buffer that contains 10 mM sodium cacodylate, 100 mM NaCl, and 0.1 mM EDTA (hereafter denoted as CNE buffer). Stock solutions of DAPI-free poly(dT) and poly(rA)·poly(dT) in either the absence or presence of DAPI (20 μM) were prepared at equivalent concentrations of 40 μM nucleotide and base pair, respectively. Portions of each solution were mixed at the appropriate volumetric ratios and, after equilibration, the absorbance at 260 nm was measured.

UV melting profiles. Absorbance versus temperature profiles were measured at 260 nm, with a heating rate of 0.1°C/min. For the ligand-dependent studies, solutions containing 1:1 stoichiometric mixtures of poly(rA)·poly(dT) and poly(dT) were 90 μM in nucleotide and contained 10 mM sodium cacodylate (pH 6.8), 100 mM NaCl, 0.1 mM EDTA, and DAPI at concentrations ranging from 0 to 30 μM. For the salt-dependent studies, solutions containing 1:1 stoichiometric mixtures of poly(rA)·poly(dT) and poly(dT) were 90 μM in nucleotide and contained 10 mM sodium cacodylate (pH 6.8), 0.1 mM EDTA, 15 μM DAPI, and NaCl at concentrations ranging from 0 to 631 mM. For each optically detected transition, the transition temperature (T_m or T_{max}) and the van't Hoff transition enthalpy (ΔH_{vH}) were determined as previously described.[54-57]

Absorption spectra. Isothermal (25 °C) absorption spectra for the linear dichroism experiments were acquired from 220 to 450 nm. The poly(rA)·2poly(dT) solution was 30 μM in base triplet and contained 15 μM DAPI, 10 mM sodium cacodylate (pH 6.8), 100 mM NaCl, and 0.1 mM EDTA. The poly(rA)·poly(dT) solution was 50 μM in base pair and contained 10 μM DAPI, 10 mM sodium cacodylate (pH 6.8), 25 mM NaCl, and 0.1 mM EDTA.

Differential scanning calorimetry (DSC)

Heat capacity (ΔC_p) versus temperature (T) profiles for the thermally induced transitions of solutions containing 1:1 stoichiometric mixtures of poly(rA)·poly(dT) and poly(dT) were measured in CNE buffer using a prototype Model 5100 Nano Calorimeter (Calorimetry Science Corporation, Provo, UT). In these experiments, the heating rate was 60 °C/h. Transition enthalpies (ΔH_{cal}) were calculated from the areas under the heat capacity curves using the Origin version 2.9 software (MicroCal, Inc., Northampton, MA). The nucleic acid solutions were 300 μM in nucleotide and contained either 0 or 100 μM DAPI.

Flow linear dichroism measurements

Flow linear dichroism measurements were conducted as previously described.[44] Each flow linear dichroism spectrum shown in panel B of Figure 6 was acquired from 240 to 450 nm and reflects the average of two scans. A Couette cell with a total optical pathlength of 1.2 mm was used for all the linear dichroism studies. The poly(rA)·2poly(dT) solution was 30 μM in base triplet and contained 15 μM DAPI, 10 mM sodium cacodylate (pH 6.8), 100 mM NaCl, and 0.1 mM EDTA. The poly(rA)·poly(dT) solution was 50 μM in base pair and contained 10 μM DAPI, 10 mM sodium cacodylate (pH 6.8), 25 mM NaCl, and 0.1 mM EDTA.

Viscometry

Viscosity measurements were conducted in a Cannon–Manning size 75 capillary viscometer (Thomas Scientific, Swedesboro, NJ) immersed in a water bath maintained at 3.5 (±0.1) °C. Flow times were multiply measured to an accuracy of ±0.3 s, and the average time over all replicates was recorded. DAPI titrations were conducted in CNE buffer by incrementally adding 3 μL aliquots of 4 mM DAPI into the viscometer containing polynucleotide solutions (1 mL) that were either 600 or 900 μM in nucleotide. Flow times ranging from 290 to 405 s were measured after each addition.

Computer modeling

Theoretical modeling of the DAPI–poly(rA)·2poly(dT) intercalation complex was conducted in two stages. The first stage entailed the identification of lowest energy triple helix conformations, in which adjacent base triplets were separated sufficiently so as to accommodate insertion of a DAPI molecule. A constrained molecular modeling method[58,59] was used to construct the triple helix. The starting coordinates of the base triplets were taken from the Arnott fiber diffraction model of the poly(dA)·2poly(dT) triplex.[60] Possible polymer building blocks that connect successive bases on each of the three strands then were identified by an exhaustive search of chain backbone conformation space. The base triplet rise was set to 6.8 Å and the helical twist angle to 10° in all structures. These values, which correspond to a helix unwinding angle of 20°, fall within the limits of the known geometries of drug–nucleic acid intercalation complexes as derived from X-ray,[61] sedimentation velocity,[62,63] and gel electrophoresis[64] studies.

The unbound polymer triplex of lowest computed potential energy then was used in positioning the DAPI molecule in the second stage of modeling. In the absence of a crystal structure for the free DAPI

molecule, starting coordinates were taken from the crystal structure of a DAPI–DNA complex in which the ligand was associated with the minor groove of the host duplex.[65] The coordinates of the drug molecule were transformed to a new reference frame in which the origin was located at the C2 atom of the indole ring and the x-axis was defined along the C2–C1′ bond (see Fig. 1). The y-axis of this reference frame coincided with the plane formed by atoms C1, C2, and C3, and the z-axis completed the right-handed coordinate reference frame (Fig. 1). The drug was initially placed in the same plane as the reference base triplet on the 5′ side of the poly(rA) strand. In this way, the DAPI reference frame was coincident with the helical reference frame.[60] A vertical translation of 3.4 Å then was introduced to place the ligand molecule approximately halfway between the reference base triplet and its neighbor. Numerous structures were generated by sequentially rotating the DAPI molecule about the x-, y-, and z-axes, as well as by sequential translations along the x- and y-axes. Rotations about the z-axis were varied in 10°-intervals from 0 to 350°. Rotations about the x- and y-axes, which are analogous to the tilting and rolling motions of a standard Watson–Crick base pair in a normal B-DNA duplex, were varied in 5°-intervals from −10° to +10°. The x and y translations were varied in 1 Å-increments from −10 Å to +10 Å. These translations facilitated the identification of an energetically stable location for the intercalating ligand within the rigid triplex framework.

At each ligand position, the total potential energy of the ligand–triplex complex was determined using standard potential energy functions. The van der Waals' contributions (both repulsive and attractive) were estimated by a combination of 6–12 and 10–12 potentials. The 10–12 potential also was used for the estimation of hydrogen bond contributions. The electrostatic energy contribution was assessed with a standard Coulombic potential.[59] The atomic charges for the DNA and RNA molecules were derived from high resolution, low temperature, single-crystal, X-ray diffraction studies of model nucleotides and nucleosides,[66] while the partial charges of the DAPI atoms were estimated using the MOPAC software.[67] To allow for a wider search of ligand placement, the interactions of drug and DNA with explicit solvent molecules were ignored. Instead, the dielectric constant, ε, was treated as a distance-dependent variable and the local ionic environment was simulated through reduction by 0.848 esu (i.e., net phosphate charge = −0.152 esu) of the net charge assigned to each phosphate group following established counterion condensation theory.[68–70] Complete parameterization of the force field is presented elsewhere.[59]

Acknowledgements

This work was supported by National Institutes of Health Grants GM20861 (W.K.O.), GM23509 (K.J.B.), GM34469 (K.J.B.), and CA47995 (K.J.B.). We are indebted to Mr Andrew J. Olson for his assistance with preparation of the computer modeling figure. We also thank Dr Helen M. Berman for graciously allowing us to conduct our viscometric studies in her cold room facility.

References

1. Wells, R. D.; Collier, D. A.; Hanvey, J. C.; Shimizu, M.; Wohlrab, F. *FASEB. J.* **1988**, *2*, 2939.

2. Hélène, C.; Toulmé, J.-J. *Biochim. Biophys. Acta* **1990**, *1049*, 99.

3. Hélène, C.; Sun, J.-S.; François, J.-C.; Saison-Behmoaras, T.; Montenay–Garestier, T.; Asseline, U.; Thuong, N. T. In *Structure & Methods*, Volume 1: Human Genome Initiative & DNA Recombination; Sarma, R. H.; Sarma, M. H., Eds.; Adenine: Schenectady, 1990; p 51.

4. Hélène, C.; François, J.-C.; Giovannangeli, C.; Saison-Behmoaras, T.; Asseline, U.; Thuong, N. T. In *Molecular Basis of Specificity in Nucleic Acid-Drug Interactions*; Pullman, B.; Jortner, J., Eds.; Kluwer Academic: Netherlands, 1990; p 291.

5. Hélène, C. *Anti-Cancer Drug Des.* **1991**, *6*, 569.

6. Thuong, N. T.; Hélène, C. *Angew. Chem. Int. Ed. Engl.* **1993**, *32*, 666.

7. Radhakrishnan, I.; Patel, D. J. *Biochemistry* **1994**, *33*, 11405.

8. Hélène, C.; Thuong, N. T.; Harel-Bellan, A. *Ann. N.Y. Acad. Sci.* **1992**, *660*, 27.

9. Minton, K. W. *J. Exp. Pathol.* **1985**, *2*, 135.

10. Cooney, M.; Czernuszewicz, G.; Postel, E. H.; Flint, S. J.; Hogan, M. E. *Science* **1988**, *241*, 456.

11. Birg, F.; Praseuth, D.; Zerial, A.; Thuong, N. T.; Asseline, U.; Le Doan, T.; Hélène, C. *Nucleic Acids Res.* **1990**, *18*, 2901.

12. Kohwi, Y.; Kohwi-Shigematsu, T. *Genes Devel.* **1991**, *5*, 2547.

13. Duval-Valentin, G.; Thuong, N. T.; Hélène, C. *Proc. Natl. Acad. Sci. U.S.A.* **1992**, *89*, 504.

14. Maher III, L. J.; Dervan, P. B.; Wold, B. *Biochemistry* **1992**, *31*, 70.

15. Grigoriev, M.; Praseuth, D.; Robin, P.; Hemar, A.; Saison-Behmoaras, T.; Dautry-Varsat, A.; Thuong, N. T.; Hélène, C.; Harel-Bellan, A. *J. Biol. Chem.* **1992**, *267*, 3389.

16. Volkmann, S.; Dannull, J.; Moelling, K. *Biochimie* **1993**, *75*, 71.

17. Skoog, J. U.; Maher III, L. J. *Nucleic Acids Res.* **1993**, *21*, 2131.

18. Moser, H. E.; Dervan, P. B. *Science* **1987**, *238*, 645.

19. Strobel, S. A.; Moser, H. E.; Dervan, P. B. *J. Am. Chem. Soc.* **1988**, *110*, 7927.

20. Boidot-Forget, M.; Chassignol, M.; Takasugi, M.; Thuong, N. T.; Hélène, C. *Gene* **1988**, *72*, 361.

21. François, J.-C.; Saison-Behmoaras, T.; Barbier, C.; Chassignol, M.; Thuong, N. T.; Hélène, C. *Proc. Natl. Acad. Sci. U.S.A.* **1989**, *86*, 9702.

22. François, J.-C.; Saison-Behmoaras, T.; Chassignol, M.; Thuong, N. T.; Hélène, C. *J. Biol. Chem.* **1989**, *264*, 5891.

23. Hélène, C.; Thuong, N. T.; Saison-Behmoaras, T.; François, J.-C. *Trends Biotech.* **1989**, *7*, 310.

24. Perrouault, L.; Asseline, U.; Rivalle, C.; Thuong, N. T.; Bisagni, E.; Giovannangeli, C.; Le Doan, T.; Hélène, C. *Nature (London)* **1990**, *344*, 358.

25. Strobel, S. A.; Doucette-Stamm, L. A.; Riba, L.; Housman, D. E.; Dervan, P. B. *Science* **1991**, *254*, 1639.

26. Shimizu, M.; Inoue, H.; Ohtsuka, E. *Biochemistry* **1994**, *33*, 606.

27. Roberts, R. W.; Crothers, D. M. *Science* **1992**, *258*, 1463.

28. Han, H.; Dervan, P. B. *Proc. Natl. Acad. Sci. U.S.A.* **1993**, *90*, 3806.

29. Escudé, C.; François, J.-C.; Sun, J.-S.; Ott, G.; Sprinzl, M.; Garestier, T.; Hélène, C. *Nucleic Acids Res.* **1993**, *21*, 5547.

30. Pilch, D. S.; Breslauer, K. J. *Proc. Natl. Acad. Sci. U.S.A.* **1994**, *91*, 9332.

31. Job, P. *Ann. Chim., Fr.* **1928**, *9*, 113.

32. Riley, M.; Maling, B.; Chamberlin, M. J. *J. Mol. Biol.* **1966**, *20*, 359.

33. Chou, W.-Y. Ph.D. Thesis, Rutgers—The State University of New Jersey, New Brunswick, 1990.

34. Breslauer, K. J.; Freire, E.; Straume, M. *Meth. Enzymol.* **1992**, *211*, 533.

35. Pilch, D. S.; Kirolos, M. A.; Breslauer, K. J. *Biochemistry* **1995**, *34*, 16107.

36. Marky, L. A.; Snyder, J. G.; Remeta, D.; Breslauer, K. J. *J. Biomol. Struct. Dyn.* **1983**, *1*, 487.

37. Marky, L. A.; Snyder, J. G.; Breslauer, K. J. *Nucleic Acids Res.* **1983**, *11*, 5701.

38. Chou, W. Y.; Marky, L. A.; Zaunczkowski, D.; Breslauer, K. J. *J. Biomol. Struct. Dyn.* **1987**, *5*, 345.

39. Park, Y.-W.; Breslauer, K. J. *Proc. Natl. Acad. Sci. U.S.A.* **1992**, *89*, 6653.

40. Park, Y.-W. Ph.D. Thesis, Rutgers—The State University of New Jersey, New Brunswick, 1992.

41. Pilch, D. S.; Kirolos, M. A.; Liu, X.; Plum, G. E.; Breslauer, K. J. *Biochemistry* **1995**, *34*, 9962.

42. Nordén, B. *Appl. Spectrosc. Rev.* **1978**, *14*, 157.

43. Wilson, R. W.; Schellman, J. A. *Biopolymers* **1978**, *17*, 1235.

44. Geacintov, N. E.; Ibanez, V.; Rougée, M.; Bensasson, R. V. *Biochemistry* **1987**, *26*, 3087.

45. Wilson, W. D.; Tanious, F. A.; Barton, H. J.; Jones, R. L.; Fox, K.; Wydra, R. L.; Strekowski, L. *Biochemistry* **1990**, *29*, 8452.

46. Tanious, F. A.; Veal, J. M.; Buczak, H.; Ratmeyer, L. S.; Wilson, W. D. *Biochemistry* **1992**, *31*, 3103.

47. Sehlstedt, U.; Kim, S. K.; Nordén, B. *J. Am. Chem. Soc.* **1993**, *115*, 12258.

48. Kim, H.-K.; Kim, J.-M.; Kim, S. K.; Rodger, A.; Nordén, B. *Biochemistry* **1996**, *35*, 1187.

49. Eriksson, S.; Kim, S. K.; Kubista, M.; Nordén, B. *Biochemistry* **1993**, *32*, 2987.

50. Bloomfield, V. A.; Crothers, D. M.; Tinoco Jr., I. *Physical Chemistry of Nucleic Acids*; Harper pp 442–445.

51. Stein, C. A.; Cohen, J. S. *Cancer Res.* **1988**, *48*, 2659.

52. Toulmé, J.-J.; Hélène, C. *Gene* **1988**, *72*, 51.

53. Kohlstaedt, L. A.; Wang, J.; Friedman, J. M.; Rice, P. A.; Steitz, T. A. *Science* **1992**, *256*, 1783.

54. Marky, L. A.; Breslauer, K. J. *Biopolymers* **1987**, *26*, 1601.

55. Breslauer, K. J. In *Thermodynamic Data for Biochemistry and Biotechnology*; Heinz, H.-J., Eds.; Springer: New York, 1986; pp 402–427.

56. Breslauer, K. J. In *Methods in Molecular Biology, Vol. 26: Protocols for Oligonucleotide Conjugates*; Agrawal, S., Eds.; Humana: Totowa, 1994; pp 347–372.

57. Breslauer, K. J. *Meth. Enzymol.* **1995**, *259*, 221.

58. Srinivasan, A. R.; Olson, W. K. *J. Biomol. Struct. Dyn.* **1987**, *4*, 895.

59. Srinivasan, A. R.; Olson, W. K. *Nucleic Acids Res.* **1997**, submitted.

60. Arnott, S.; Bond, P. J.; Selsing, E.; Smith, P. J. C. *Nucleic Acids Res.* **1976**, *3*, 2459.

61. Berman, H. M.; Young, P. R. *Annu. Rev. Biophys. Bioeng.* **1981**, *10*, 87.

62. Crawford, L. V.; Waring, M. J. *J. Mol. Biol.* **1967**, *25*, 23.

63. Bauer, W.; Vinograd, J. *J. Mol. Biol.* **1968**, *33*, 141.

64. Keller, W. *Proc. Natl. Acad. Sci. U.S.A.* **1975**, *72*, 4876.

65. Larsen, T. A.; Goodsell, D. S.; Cascio, D.; Grzeskowiak, K.; Dickerson, R. E. *J. Biomol. Struct. Dyn.* **1989**, *7*, 477.

66. Pearlman, D. A.; Kim, S.-H. *J. Mol. Biol.* **1990**, *211*, 171.

67. Stewart, J. J. P. *J. Comput. Chem.* **1989**, *10*, 209.

68. Manning, G. S. *Q. Rev. Biophys.* **1978**, *11*, 179.

69. Record, M. T., Jr.; Anderson, C. F.; Lohman, T. M. *Q. Rev. Biophys.* **1978**, *11*, 103.

70. Srinivasan, A. R.; Olson, W. K. *Fed. Proc.* **1980**, *39*, 2199.

(*Received in U.S.A.* 8 *October* 1996; *accepted* 18 *February* 1997)